JOURNAL OF MATERIALS SCIENCE 18 (1983) 1999–2010

Imaging of polyethylene films by diffraction contrast

V. P. CHACKO*, W. W. ADAMS†, E. L. THOMAS
Polymer Science and Engineering Department, University of Massachusetts, Amherst, Massachusetts 01003, USA

The technique of crystalline diffraction contrast imaging of lamellae in spherulitic and oriented thin films of polyethylene is illustrated for both conventional transmission and scanning transmission electron microscopy. Bright-field "ghost" imaging permits real space crystallography of the specimen and reveals the occurrence of variable chain inclination in a given lamellar preparation. N beam annular dark-field scanning transmission microscopy is useful for distinguishing between curved lamellae and mosaic blocks as well as for the direct imaging of the amorphous regions between lamellae.

1. Introduction

There continues to be a strong interest in the study of the microstructural organization of melt-crystallized polyethylene (PE). Typical investigations use scattering methods (X-ray, neutron) or microscopy for the objective of determining how macromolecules are organized into lamellar crystals and how lamellae are organized into higher order structures such as spherulites and oriented films.

Electron microscopy studies of polyethylene frequently involve either replication techniques or staining techniques. These methods are employed because of the difficulty of preparing thin sections of polyethylene and because the polymer is rapidly damaged by the electron beam at the current densities usually employed in conventional transmission electron microscopy (CTEM) [1]. This deterioration has two aspects: (a) loss of crystallinity; and (b) sample distortion resulting from thinning of lamellae in the chain axis direction and expansion in the other directions. Therefore, electron damaged specimens do not convey an accurate image of the micromorphology. Staining, especially that involving chlorosulphonation [2] can prevent much of the distortion of the thin film during electron exposure (provided careful low-intensity techniques are employed) and permits detailed examination of the local morphology primarily by use of mass thickness contrast. Staining techniques, along with replication and small-angle scattering have been used to understand the effects of crystallization temperature, molecular weight, pressure and other intrinsic and extrinsic parameters on the micromorphology of polyethylene [3–5]. Chlorosulphonation, however, can lead to significant dimensional changes (a 30% shrinkage!) in the lamellar spacing of polypropylene [6]. Thus, the electron microscopic study of untreated crystalline thin films or sections in addition to permitting the observation of unaltered specimens, has advantages not realizable with treated or replicated specimens. Most importantly, the sample crystallinity permits the use of a variety of microscopic imaging modes: bright-field imaging (BF), dark-field imaging (DF) and selected-area diffraction (SAD) or micro-beam diffraction (MBD), to obtain complementary images as well as crystallographic orientation of regions in the film.

For radiation sensitive polymers, scanning transmission electron microscopy (STEM) techniques facilitate consecutive imaging of a region of a polymer crystalline thin film. This permits variation of the diffraction conditions to enable systematic studies of the crystalline contrast

*Permanent address: Plastics Technical Laboratory, Allied Chemical Corporation, Morristown, New Jersey 07960, USA.
†Permanent address: Polymer Branch, Materials Laboratory, Wright-Patterson Air Force Base, Ohio 45433, USA.

0022–2461/83 $03.00 + .12

mechanisms in polymeric thin films, a procedure which is quite difficult with CTEM. The advantages of STEM techniques for polyethylene have been demonstrated by Low *et al.* [7] as well as in papers from this laboratory [8–10].

The objective of this paper is to examine crystalline contrast in thin films of polyethylene and to note some deductions that can be made about the lamellar structure.

2. Experimental techniques

Thin spherulitic films of Marlex® 6003 ($\bar{M}_w$ = 200 000, MWD = 7–13 and Hifax® 1900, an ultra-high molecular weight linear polyethylene ($M_w = 2.0 \times 10^6$, MWD = 4.6) were prepared for microscopy by the following method: a dilute solution of the polyethylene (0.2%) was prepared in previously filtered, dried xylene and drops of the hot solution were placed on to the surface of glycerol kept at 140° C. After all the xylene had evaporated, the glycerol and polyethylene film were transferred to a Mettler FP-2 hot stage. The film was heated to 160° C for 15 min and then rapidly (1° C sec^{-1}) cooled to 120° C. The crystallized thin films were then transferred on to distilled water, washed and then picked up on grids. At all stages of preparation, care was taken to avoid oxidation by using a nitrogen blanket.

Thin oriented films of the Marlex® and Hifax® polyethylenes were prepared by drawing from a thin molten layer of polymer on a glass surface maintained at 130° C following the method of Petermann and Gohil [11]. When the film is drawn off the heated surface it simultaneously undergoes high deformation and rapid cooling, resulting in high orientation. Samples were subsequently annealed at 120° C for 2 h and then lightly coated with evaporated carbon before examination.

CTEM and STEM of the thin polyethylene films were performed using a JEOL 100 CX "TEMSCAN". For CTEM, micrographs of specimen areas with minimum electron damage were obtained by focusing on an area, translating to an adjacent area and recording the image on Kodak S0163 plates using approximately 60% of the crystal lifetime dose. DF imaging was obtained by tilting the incident beam so that the objective aperture selected the reflection of choice.

For STEM BF and DF imaging a 20 μm diameter second condenser aperture was used to limit incident beam divergence. Details of the STEM optics are given in the section on STEM imaging and in a previous paper [9]. Polaroid type 55 P/N film was employed.

3. Diffraction contrast

Bright-field diffraction contrast derives from scattering of the diffracted beams outside the objective aperture by crystalline regions in the sample and therefore will be limited by the radiation lifetime of the polymer. BF diffraction contrast occurs in all regions of the specimen where the Bragg condition is satisfied. DF imaging uses Bragg diffracted electrons from particular sets of crystallographic planes.

The diffraction or Bragg condition can be expressed as a vector equation:

$$\mathbf{K} - \mathbf{K}_0 = \mathbf{g}, \qquad (1)$$

where $\mathbf{K}_0$ and $\mathbf{K}$ are unit vectors of the incident and scattered beams and $\mathbf{g}$ is the reciprocal lattice vector of the operating reflection. Contrast arises from the local deviation of the lattice planes from the Bragg angle (see Fig. 1a). The diffracted

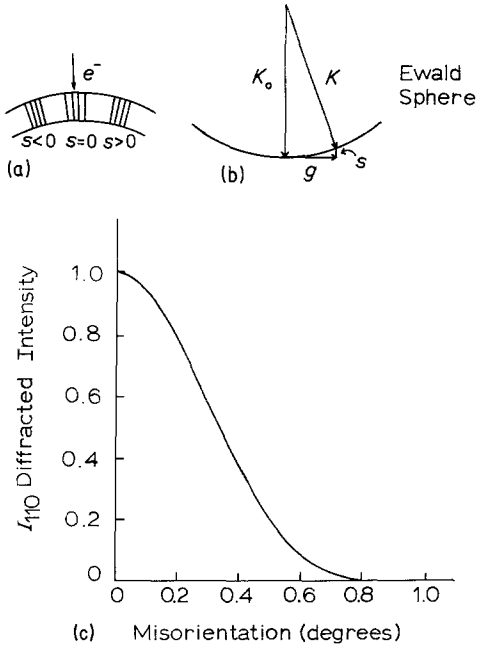

Figure 1 (a) Schematic drawing of a uniformly bent crystal showing planes oriented properly for diffraction ($s = 0$) and for nondiffraction ($s < 0, s > 0$). (b) Schematic drawing of the diffraction condition: K_0 is the incident beam vector, K the diffracted beam vector, g is the reciprocal lattice vector for a particular reflection, and s is the deviation parameter. (c) Rocking curve (1 1 0) for a 30 nm thick polyethylene single crystal.

intensity varies as

$$I(s) \simeq |F(hkl)|^2 \frac{\sin^2 \pi st}{\sin^2 \pi s} \quad (2)$$

where $F(hkl)$ is the structure factor for the (hkl) reflection, t is the crystal thickness parallel to the optic axis and s is the deviation of the (hkl) planes from the Bragg condition ($s = 0$). The relationship of s and the diffraction vector, g, and the Ewald sphere can be seen in Fig. 1b. The variation of diffracted intensity with misorientation from the Bragg condition, the so-called "rocking curve", is illustrated in Fig. 1c for the (1 1 0) reflection of a 30 nm thick polyethylene crystal. The diffracted intensity falls to zero for less than one degree of misorientation. Strain fields cause displacements of the lattice planes and affect the local diffracted intensity accordingly. Specimen texture will cause overall displacements of arrays of crystals from the Bragg condition. By using different sets of diffracting planes (different g vectors) to form DF images of the same region, it is possible to map out the strength and symmetry of the displacement field and understand details of the defects or textures present. The chief advantages of DF are the high image contrast and the direct interpretation afforded diffraction contrast features in the image. The disadvantage (particularly for single-beam DF) is the much lower diffracted intensity compared to the transmitted beam intensity.

For the BF image, the intensity can be expressed as

$$I = I_0 - \sum_g I_g \quad (3)$$

where I_0 is the incident intensity and the summation is over all the Bragg reflections active for the particular crystal orientation.

Table I presents calculated structure factors for the prominent PE reflections for 100 KeV electrons. The two strongest reflections are from the (1 1 0) and (2 0 0) planes. Therefore, regions of crystal with (0 0 l) orientation, i.e. with the chain direction parallel to the beam, will generally appear darker in bright-field than regions in any other orientation (assuming for comparison, equal film thickness of each region and all $s_g = 0$ for a particular crystal orientation).

TABLE I Structure factors for selected polyethylene reflections*

hkl	2θ (mrad)	d_{hkl} (nm)	F^2 (nm^2)	F^2/F^2_{110}
1 1 0	9	0.410	0.92	1.00
2 0 0	10	0.369	0.69	0.74
0 2 0	15	0.246	0.28	0.30
0 0 2	29	0.127	0.18	0.19
2 0 1	18	0.209	0.16	0.17
0 1 1	16	0.225	0.15	0.16
1 2 1	22	0.172	0.13	0.14
4 0 0	20	0.185	0.13	0.14
0 3 1	27	0.138	0.11	0.12
3 1 0	17	0.220	0.10	0.11

*100 KeV electrons assuming scattering from 4 carbon and 8 hydrogen atoms per unit cell.

4. CTEM imaging

Fig. 2a is a CTEM BF image showing diffraction contrast banding of polyethylene spherulites grown from the Marlex® polymer. Contrast arises from the alternating orientation of the lamellae with respect to the incident electron beam along the radial directions. Fig. 2b shows similar diffraction contrast banding in a Hifax® thin film. In Fig. 2c, also of the Hifax® polymer, the lamellae are particularly well defined whenever the crystal orientation is near $(h00)$, i.e. the **b**- and **c**-axes lie in the plane of the film, normal to the electron beam direction. Such clear distinction of the lamellae in unstained, spherulitic films is not, as far as we know, noted in the literature. The good definition achieved in Hifax® is due to the relatively high amorphous content (~ 40% by DSC measurement) which lies predominantly between lamellae.

Both BF and DF CTEM images of polyethylene lamellae in spherulites and oriented films are quite common in the literature. One feature is worthy of further comment. In many BF micrographs there appear regions where two or three lines of strong contrast intersect at a common point, giving the impression of a cross or star (see for example, the regions in Fig. 2c and in Figs. 5a and 7). It will be shown in the section on STEM annular DF imaging that these type of diffraction contrast features are bend contours which can arise due to lamellar curvature.

5. Ghost images

A somewhat more novel CTEM diffraction contrast feature is that of bright-field "ghost" images. Keller *et al.* [12], in an early study of polyethylene single crystals, showed that such white diffraction images are seen whenever the objective lens is defocused and no (or a large) limiting objective

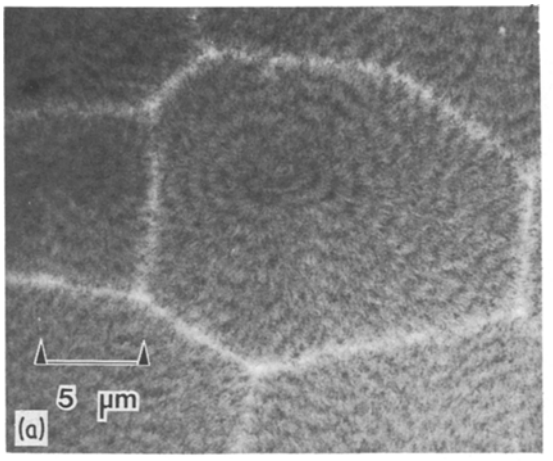

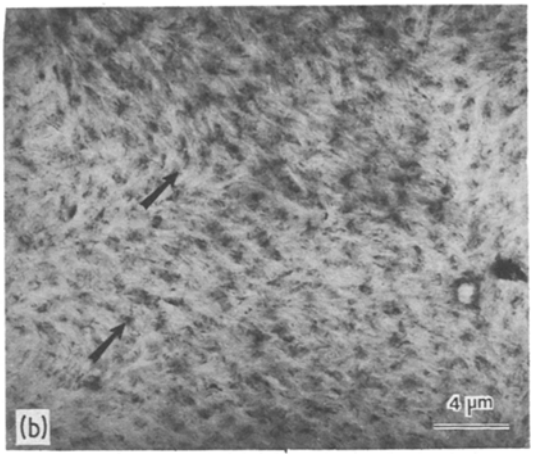

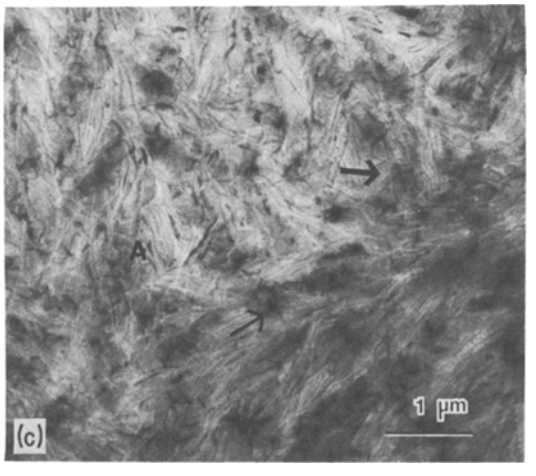

Figure 2 (a) CTEM BF micrograph of a Marlex® thin film spherulite showing diffraction contrast banding. Light regions are spherulite boundaries. (b) CTEM BF micrograph of less organized banding (arrowed) in a Hifax® film. (c) CTEM BF micrograph at higher magnification of the Hifax® film. Arrows point to several cross bend contours.

aperture is used (Fig. 3a). In a focused BF image, spherical aberration causes the diffracted beam (dark-field) images from a crystal to rejoin the unscattered beam (bright-field) image with a slight lateral shift given by $\Delta x = C_s(2\theta)^3$ (e.g. for a spherical aberration coefficient $C_s = 6$ mm, $\Delta x \simeq 5$ nm for 110 PE reflection at 100 KV). This image defect in CTEM is of no consequence when a limiting objective aperture is employed, but it can be used to determine the C_s for a particular objective lens pole piece [13]. When a defocus Δf (in the object plane) is introduced, the various diffraction images shift by an additional amount given by $\Delta f \cdot 2\theta$, in the direction of the respective operating g vectors. Note that further variation in Δx will occur in a field of view if the sample is tilted with respect to plane of focus. Thus, the total image shift for a ghost image is given by

$$\Delta x(\mathbf{r}) = C_s(2\theta)^3 + \Delta f(\mathbf{r})2\theta, \qquad (4)$$

where $\Delta f(\mathbf{r})$ is the positional dependent defocus.

In bright-field ghost imaging, the simultaneous presence of bright- and dark-field images provides a real space method to describe the orientation of particular diffracting crystallites.

Care must be taken to correct objective lens astigmatism, since this will result in variable shift lengths of the diffraction images for different crystal orientation. In addition, if an objective aperture is used, it must be carefully centred, since one reflection of a Friedel pair may be blocked while the other forms a single diffraction image.

For example, consider a polyethylene lamella oriented such that the electron beam is normal to the **b**- and **c**-axes ($(h00)$ orientation). The diffraction pattern for such a crystal will be the $(0kl)$ reciprocal lattice. The three most prominent reflections in this section of reciprocal space are the (020), (011) and (002). Each set of planes diffracting in the crystal will give rise to two ghost images (one each for $\pm g$) displaced exactly the same distance from the bright-field image but in opposite directions. If the crystal is oriented such that the deviation parameter s_g is zero for all three reflections, six ghost images will be produced. For a given Δf, the image shifts will be in the approximate ratio of 1 : 1.1 : 2 (see Fig. 3b). Since normally only a few crystals in a given field are diffracting simultaneously, ghost images provide a means to obtain selective local crystal orientation without the need for successive

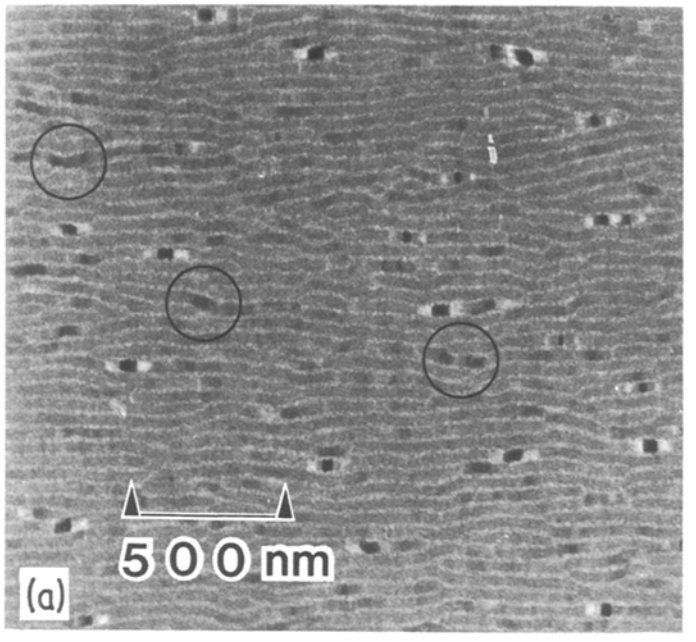

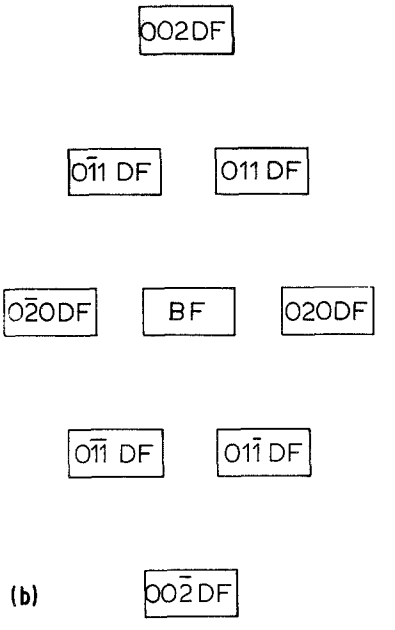

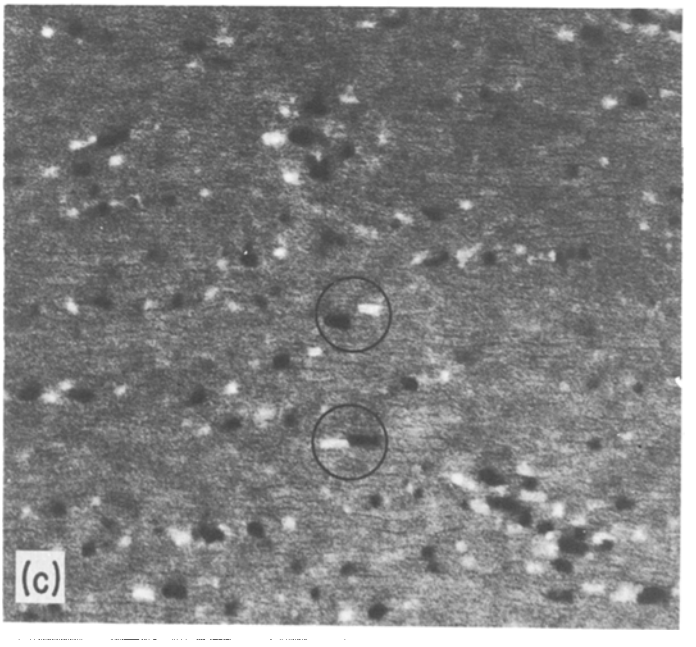

Figure 3 (a) CTEM BF ghost image of oriented polyethylene film (underfocused). Circled regions are crystals oriented for other than (1 1 0)/(2 0 0) diffraction. (b) Schematic illustration of ghost image pattern expected for a single lamella oriented (*h* 0 0). (c) CTEM BF ghost image of oriented polyethylene film (overfocused). Circled regions show variation of image shift of (1 1 0)/(2 0 0) diffracting regions indicating variation of chain tilt angle.

microarea electron diffraction patterns or sequential single-beam DF images which are difficult to obtain for radiation-sensitive crystals approaching the size of typical polymer lamellae. Since this real space crystallography method identifies the particular region of the crystal oriented for diffraction from a particular set of planes, crystal bending may be mapped by monitoring the positional variation in the diffracted intensity for the various ghost images.

It should be noted that the ghost image technique is essentially the same approach as the defocus multiple dark-field image technique recently applied to polymers by Lovinger and Keith [14]. In this technique, the selected-area diffraction pattern is spread into discs by defocusing of the intermediate lens. Each of the non-central discs is a dark-field image which corresponds to the particular Bragg reflection while the central disc is the bright-field image. As is the

case for ghost images, the image array provides simultaneous rather than sequential information which is beneficial for radiation sensitive polymers. Unfortunately, the multiple dark-field images are also aberrated by the defocus employed. Ignoring radiation damage effects, the image resolution in both the ghost and multiple dark-field image techniques is determined by the incident beam divergence combined with objective lens spherical aberration and more importantly image defocus. In order to sufficiently displace the various dark-field images from the bright-field images, a defocus equal to $p/2\theta$ is required where p is the centre-to-centre spacing of the image discs in the multiple dark-field technique or the centre-to-centre image shift in the ghost image technique. The defocus limited resolution is given by $\Delta f \Delta\alpha$, where $\Delta\alpha$ is the incident beam divergence in radians. In the multiple DF technique, for 1 μm area discs (corresponding to the smallest practical SAD aperture) separated to just-touching, the required Δf is about 10^5 nm. For a typical beam divergence of 10^{-4} radians, the divergence smearing resolution limit is about 10 nm. For ghost images of lamellae, the necessary defocus can be much less since now only the individual object images need to be separated to just-touching. For 100 nm long lamellae, this would necessitate a defocus of about 10^4 nm, improving the divergence limited resolution to about 1 nm.

Fig. 3a and c are BF CTEM ghost images of an oriented Marlex® film prepared following the method of Petermann and Gohil [11]. Examination of the direction and magnitude of the image shift and the image intensity indicates only the (110) and (200) reflections produce readily visible ghost images. Distinction between these two reflections is difficult at the resolutions obtainable since their respective shift direction and magnitude and image intensity are very similar. Regions displaying symmetrical ghosts are oriented precisely at the Bragg condition. Note that the width of the diffracting regions varies from 10 to 80 nm. While other planes do diffract (see circled regions), their ghost images are unfortunately imperceptable in the phase-contrast background of alternating amorphous and crystalline lamellar regions. Occasionally, the (110) and (200) ghost images are observed to shift at an angle to the BF image of the lamella (see arrowed regions in Fig. 3c). Such nonparallel shifts indicate that the diffracting planes are inclined to the lamellar surface normal. Since the chain axis in PE is parallel to the (110) and (200) planes, the chains are therefore oblique to the lamellar surface normal. Chain obliquity is a common feature in polyethylene and has been measured in individual single crystals by DF CTEM tilt experiments [15] and an average value for the bulk can be deduced from X-ray diffraction methods and low-frequency Raman spectroscopy [16].

Inspection of (110)/(200) ghost image shifts show a variation in angle from 0° up to about 22°. This is direct evidence of the occurrence of variable chain inclination in a given lamellar preparation. Voigt-Martin *et al.* [17] have also recently identified the occurrence of different surface planes even within single lamella employing CTEM BF imaging of stained PE films. Such variation of chain tilt has important implications for the correct determination of the crystal core thickness, crystalline stem length and long-period distributions obtained from models assuming constant chain obliquity for all lamellae.

It is also interesting to note the reversal of the phase contrast of the amorphous and crystalline regions in the overfocused image (Fig. 3c) compared to the underfocused image (Fig. 3a). Ongoing studies of phase-contrast imaging employ the magnitude of the ghost image shifts to determine local values of specimen defocus [18].

6. STEM imaging

Imaging of radiation sensitive polymers is much easier with STEM primarily because of image intensification and higher collection efficiency of scattered electrons. Another disadvantageous feature that we demonstrate here is the flexibility of imaging. It is possible to vary the optical parameters of the STEM to permit novel DF imaging modes. Use of the sample z-axis lift and intermediate lens current control permits variation of the camera constant. In addition, the use of a modified beam stop tip and various SAD apertures effectively converts the photomultiplier tube detector into a number of detectors with differing geometry and size.

Fig. 4a to f shows schematic illustrations of the optics and the resultant microdiffraction pattern intensity distribution at the detector (utilizing an oriented PE film) for some optical arrangements which can be utilized for BF and DF STEM. For BF, diffraction contrast is pro-

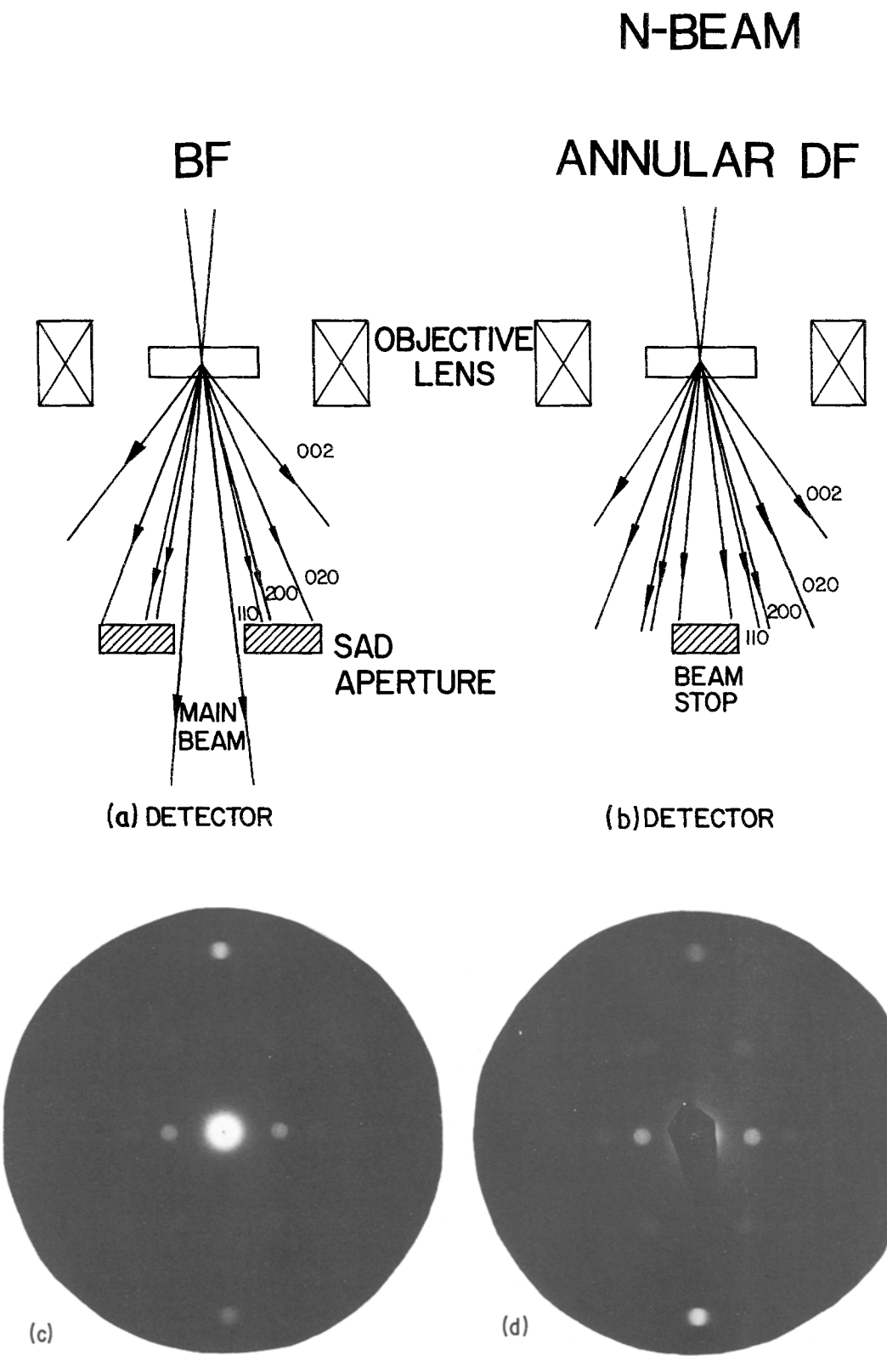

Figure 4 Schematic drawings of various STEM detector geometries and microdiffraction patterns. (a) STEM BF. (b) STEM n-beam annular DF. (c) Micro-micro diffraction pattern of oriented Marlex® PE film. (d) Micro-micro diffraction pattern for n-beam annular DF. (e) STEM 002 annular DF. (f) Micro-micro diffraction pattern for 002 annular DF.

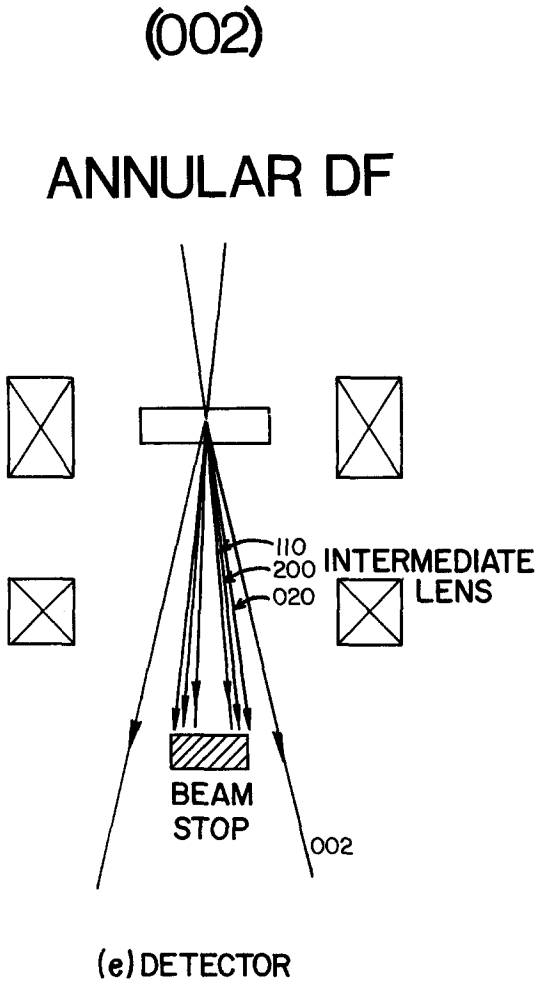

vided by blocking almost all the scattered electrons with an SAD aperture (see Fig. 4a). For n-beam annular DF, the main beam is blocked by a modified beam stop and all other reflections out to some cut-off angle (determined by the SAD or column apertures) are collected (see Fig. 4b and d). For example, in (110)/(200) annular DF, the main beam as well as all other reflections are blocked using the beam stop and a larger diameter SAD aperture. For (002) annular DF, the intermediate lens current is adjusted to decrease the camera constant so as to collapse all the inner reflections into the beam stop, effectively allowing only the (002) reflection and other higher angle, weaker reflections to form the image (see Fig. 4e and f).

Four consecutive STEM images from the same area of a Hifax® spherulitic film utilizing the various optical modes are shown in Fig. 5a to d. The BF and n-beam annular DF images are, as expected, complementary – the dark diffracting

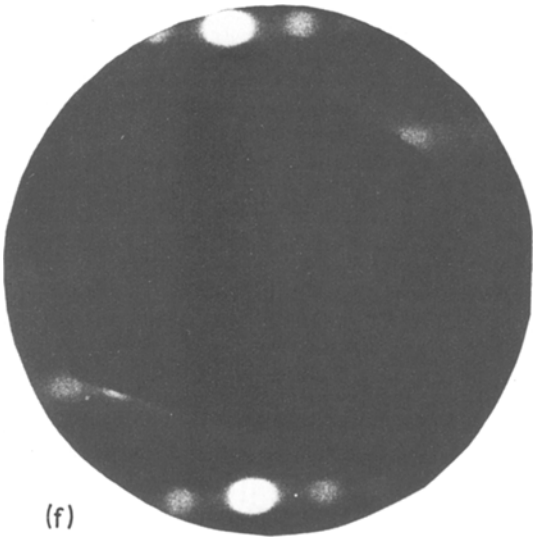

Figure 4 Continued.

regions in the BF (Fig. 5a) correspond to the bright diffracting regions in the DF image (Fig. 5b). The (110)/(200) annular DF (Fig. 5c) and the (002) annular DF images (Fig. 5d) were taken at higher magnification (and hence are somewhat more noisy due to lower diffracted electron signal and accumulated electron beam damage) and show the portion of the field of view indicated by the white box in Fig. 5a. The (110)/(200) annular DF image shows those regions of the film with (00*l*) orientation. Dark regions in the DF image occur because such regions are either not at the Bragg condition for the reflection(s) employed or they are noncrystalline. Some of the long, narrow dark regions in the (110)/(200) annular DF image appear as bright diffracting regions in the (002) annular DF image indicating these regions are lamellae oriented edge-on for (002) diffraction. Since in STEM annular DF, the entire azimuthal distribution of diffracted intensity of a reflection is employed, all azimuthal orientations of the lamellae at the Bragg angle will be imaged.

Fig. 6a is an n-beam STEM annular DF micrograph of another region of a spherulitic Hifax® film containing stacks of long thin lamellae. The bright regions are due to diffraction from the (110) and (200) planes. In addition to the bright diffracting regions, there are long continuous dark regions parallel to and alternating with somewhat thinner regions of intermediate intensity (labelled A). Since the dark regions are locally colinear with the bright diffracting regions, and become bright with appropriate specimen tilt, the dark regions

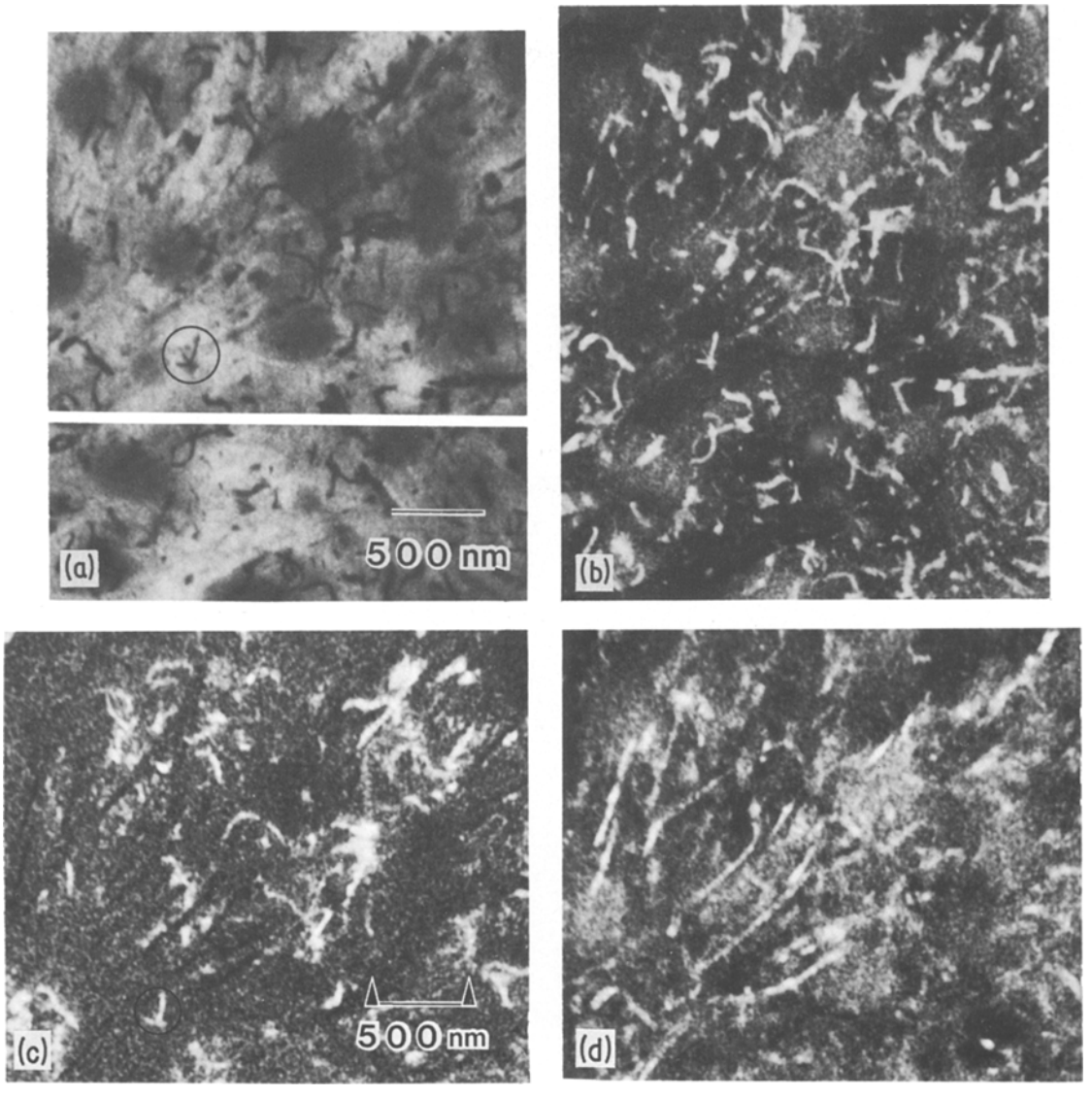

Figure 5 Consecutive STEM images of a Hifax® spherulitic film. (a) STEM BF. Symmetrical bend contour region is circled. (b) STEM n-beam annular DF. (c) STEM (1 1 0)/(2 0 0) annular DF. (d) STEM (0 0 2) annular DF.

represent crystalline lamellae not properly oriented to scatter into the region of reciprocal space selected by the annular detector (~ 2 to $3\,nm^{-1}$). The long, thin grey regions are proposed to be amorphous interlamellar zones, made visible from other nondiffracting crystalline regions by the high collection efficiency of the STEM annular detector for the amorphous halo (centred at $2.2\,nm^{-1}$).

It is interesting that most of the widths of the diffracting lamellae are greater than the widths of the dark nondiffracting lamellar regions. A possible explanation of this effect is shown schematically in Fig. 6b. The lamellae are depicted with a slight tilt with respect to the film plane such that the projected diffracting crystalline images are wider than the projected non-diffracting regions due to the intensity contribution of the intervening amorphous regions. Variation of lamellar width and tilt angle can account for side-by-side images of crystalline regions with no apparent interlamellar amorphous zone (see arrowed regions in Fig. 6a).

Ghost image shifts from CTEM BF images (see Fig. 6c) confirm the prominent diffracting regions are from the (1 1 0) and (2 0 0) planes. Furthermore, the phase-contrast image nicely

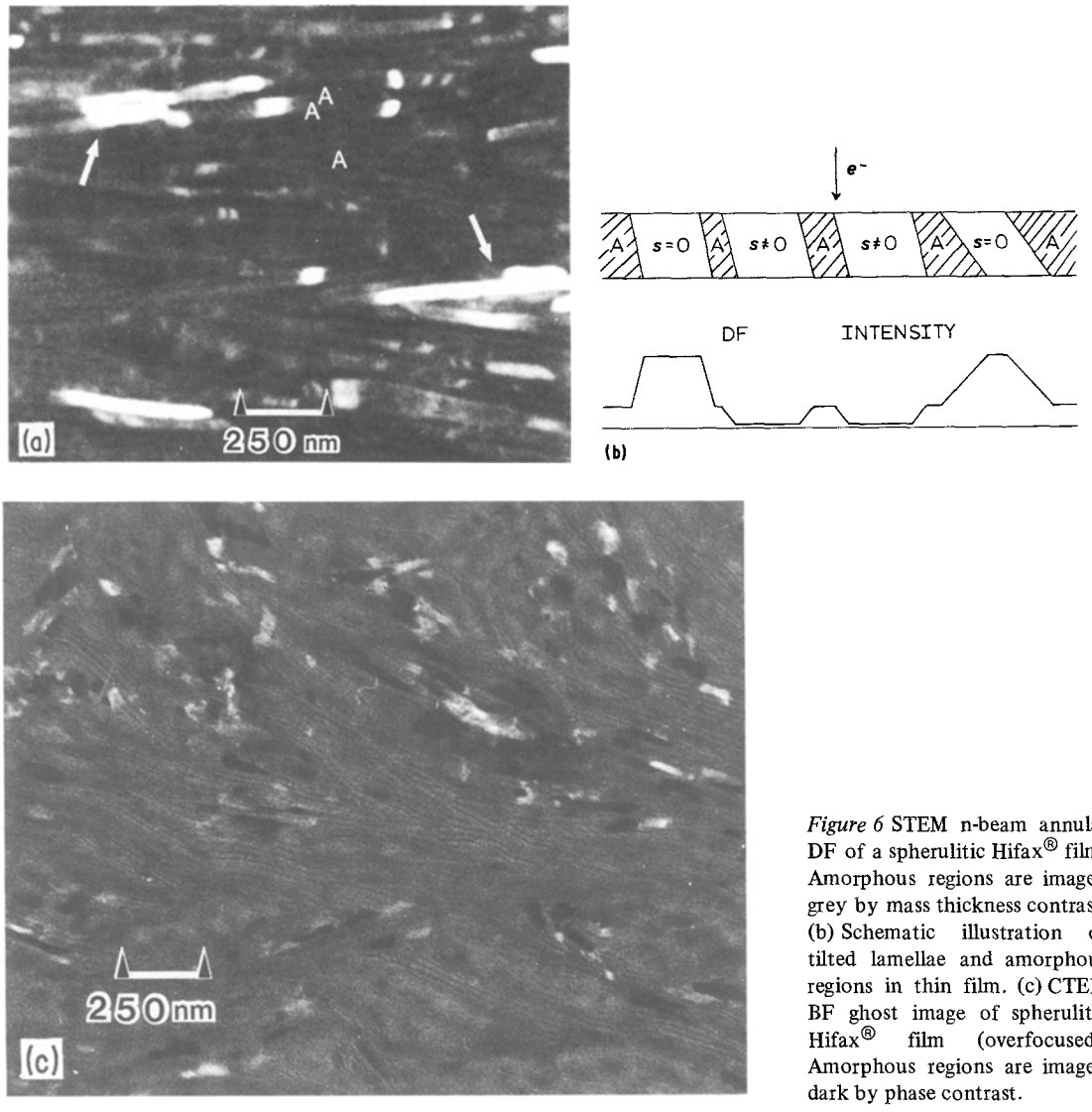

Figure 6 STEM n-beam annular DF of a spherulitic Hifax® film. Amorphous regions are imaged grey by mass thickness contrast. (b) Schematic illustration of tilted lamellae and amorphous regions in thin film. (c) CTEM BF ghost image of spherulitic Hifax® film (overfocused). Amorphous regions are imaged dark by phase contrast.

delineates the intervening amorphous regions (dark regions in this overfocussed image) in those portions of the film having lamellar arrangements as in Fig. 6c.

Fig. 7a and b are (110)/(020) annular DF micrographs illustrating the cross and star bend contours. The origin of these contrast features can be understood assuming that the diffracting lamella is oriented exactly (00*l*) at the position where the contours intersect and is approximately uniformly curved about this position (i.e. sections through the lamella appear as in Fig. 1a). Since a misorientation of greater than about 1° places the crystal out of the diffraction condition, uniform bending results in $s = 0$ conditions along radial sectors for the various ($hk0$) reflections. The three strong ((110), (200) and (020)) reflections thus give rise to the multiple symmetrical bend contours. Asymmetric bending of the lamella results in distortion of the contours. The bright contours in Fig. 7 have been labelled assuming the **b**-axis is the growth direction (long dimension of lamellae). The measured angle between the assumed (110) and (200) contours of 60° compares favourably with the calculated value for symmetrical bending of 56°, and the angle between the (200) and (020) contours is 95°, nearly the expected value of 90°. Revol *et al.* [19] have also noted the presence of "long curved streamers ... frequently cross(ing) at a common point" in BF CTEM images of annealed nascent polyethylene films. Examination of their Fig. 7 in the light of

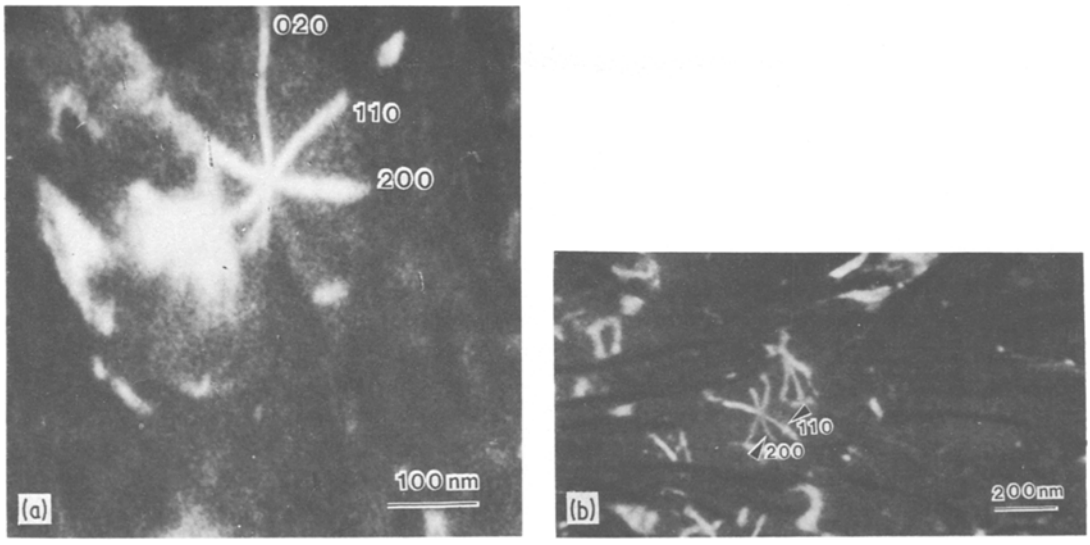

Figure 7 (a) and (b) STEM (110)/(200)/(020) annular DF micrographs of spherulitic Hifax® film containing symmetrically bent lamellae.

the present results, indicates the "streamers" are $(hk0)$ bend contours. One may estimate the curvature of the $(00l)$ oriented lamellae from the lateral extent of the bend contours and the angular width of the rocking curve assuming uniform bending. The very approximate value is $0.1^\circ\,nm^{-1}$. This is in the same order of magnitude of curvature of the S-shaped polyethylene lamellae studied by Voigt-Martin *et al.* [4] and Bassett and Hodge [3].

These rather well-defined CTEM and STEM diffraction contrast BF and DF images can also be examined to assess the size of any lamellar mosaic block substructure that may be present in these melt-crystallized thin films. The mosaic block model of polymer lamellar crystals depicts a substructure of the order of 30 nm lateral extent with tilts between neighbouring blocks of 0.6° to 11° to account for the observed X-ray diffraction line broadening [20]. The rocking curve of Fig. 1b shows the expected variation of diffracted intensity as a function of tilt away from the Bragg condition. Considering the size of the mosaic blocks and the large tilts associated with them, diffraction contrast microscopy should reveal their presence.

In BF, the diffracting blocks would appear as dark regions within the lamellae and in DF one would expect both black (nondiffracting) and white (diffracting) regions. From the present results it is evident that the lamellae in the spherulitic films are quite different from those in the oriented films in terms of a mosaic block substructure. In the spherulitic films, continuous $(hk0)$ blend contour lengths range up to 400 nm, indicating long-range perfection of the crystal lattice. However, in the oriented films one does observe the several micron long continuous lamellae to consist of much shorter $(hk0)$ diffracting regions, ranging from 10 nm up to 100 nm in length. Current line broadening measurements on stacks of the oriented films yields for example, an average crystallite size from the 110 peak of about 35 nm [20]. Direct visualization of the individual diffracting units by electron microscopy reveals the extremely wide distribution of crystallite sizes present.

Acknowledgements

We thank Mr D. Yang for providing the oriented thin films of polyethylene. Acknowledgement is made to the National Science Foundation for financial support (grant DMR 80-12724, Polymers Program (WWA and ELT), and AFOSR Grant 80-0101 (VPC). The use of the facilities of the Materials Research Laboratory at the University of Massachusetts is also gratefully acknowledged.

References

1. D. T. GRUBB, *J. Mater. Sci.* **9** (1974) 1715.
2. G. KANIG, *Kolloid Z. Z. Polymere* **251** (1973) 782.
3. D. C. BASSETT and A. M. HODGE, *Proc. Roy. Soc. (Lond.)* **A359** (1978) 121.
4. I. G. VOIGT-MARTIN, E. W. FISCHER, L. MANDELKERN, *J. Polymer Sci. (Phys)* **18** (1980)

2347.
5. D. T. GRUBB and A. KELLER, *ibid.* **18** (1980) 207.
6. N. STRIBECK, PhD Dissertation, University of Marburg (1980).
7. A. LOW, D. VESELY, P. ALLAN and M. BEVIS, *J. Mater. Sci.* **13** (1978) 711.
8. E. S. SHERMAN and E. L. THOMAS, *ibid.* **14** (1979) 1109.
9. E. S. SHERMAN, W. W. ADAMS and E. L. THOMAS, *ibid.* **16** (1981) 1.
10. V. P. CHACKO, F. E. KARASZ, R. J. FARRIS and E. L. THOMAS, *J. Polymer Sci. (Phys.)* **20** (1982) 2177.
11. J. PETERMANN and R. M. GOHIL, *J. Mater. Sci.* **14** (1979) 2260.
12. A. W. AGAR, F. C. FRANK and A. KELLER, *Phil. Mag.* **4** (1959) 32.
13. C. E. HALL, "Introduction to Electron Microscopy" 2nd edn. (McGraw Hill, New York, 1966).
14. A. J. LOVINGER and H. D. KEITH, *J. Polymer. Sci. (Phys.)* **19** (1981) 1163.
15. A. KELLER, *Rep. Prog. Phys.* **31** (1969) 623.
16. J. DLUGOSZ, G. V. FRASER, D. T. GRUBB, A. KELLER, J. A. ODELL and P. L. GOGGIN, *Polymer* **17** (1976) 471.
17. I. G. VOIGT-MARTIN, L. MANDELKERN and E. W. FISCHER, Proceedings of 28th IUPAC Macromolecular Symposium (Amherst, USA), Vol. 21 (1982).
18. D. L. HANDLIN and E. L. THOMAS, unpublished results (1982).
19. J.-F. REVOL, W. LUK and R. H. MARCHESSAULT, *J. Crystal Growth* **48** (1980) 240.
20. R. HOSEMANN, W. WILKE and F. J. BALTÁ CALLEJA, *Acta Crystallogr.* **21** (1966) 118.
21. D. YANG and E. L. THOMAS, to be published.

Received 26 July
and accepted 31 August 1982